PROCEEDINGS OF ECOS 2023 - THE 36TH INTERNATIONAL CONFERENCE ON
EFFICIENCY, COST, OPTIMIZATION, SIMULATION AND ENVIRONMENTAL IMPACT OF ENERGY SYSTEMS
25-30 JUNE, 2023, LAS PALMAS DE GRAN CANARIA, SPAIN

Optimization of a Horizontal Entrained Flow Plasma Gasification Test Rig through CFD-Simulation

Sebastian Bastek[a], Mariam Fahmy[a], Sebastian Wilhelm[a], Sebastian Fendt[a] and Hartmut Spliethoff[a]

[a] Chair of Energy Systems, Technical University of Munich, Garching, Germany, sebastian.bastek@tum.de, CA

Abstract:

Plasma gasification is a promising method for the thermochemical conversion of biomass and wastes into high quality syngas with lower tar content and higher energy densities compared to conventional processes. This study aims to optimize a horizontal tubular entrained flow plasma gasification test rig which should produce plasma pyrolysis chars. Therefore, mixing of fuel particles in the plasma zone as indicated by the respective particle temperatures needs to be improved. For that a couple of configurations were investigated by a CFD simulation in Ansys Fluent: First, the plasma torch gas outlet diameter of 1mm was doubled to reduce plasma gas velocities. Then, several vertical fuel particle inlet tubes were integrated at different distances from the plasma torch nozzle (5, 15, 25 and 35mm) to insert fuel particles more directly into the plasma zone. The wider nozzle outlet diameter resulted in higher particle temperatures, lower velocities and better convergence. From the different particle tube configurations, the closest to the plasma inlet, resulted in the highest average particle temperatures, residence times and better distribution in the reactor than the other cases. It was subsequently concluded that the optimal configuration for enhanced particle heating and mixing shall be designed with a 2mm wide diameter and a 49mm long tube that is 5 mm away from the torch outlet.

Keywords:

CFD; Plasma gasification; Entrained flow gasification; Biomass.

1. Introduction

The demand for biomass as a renewable energy source for heat and energy production as well as a source of sustainable carbon for the chemicals and materials industry is expected to increase strongly over the next decades [1]. Therefore, conversion processes are needed which achieve high efficiencies in terms of their feedstock utilization. One approach for the conversion of biomass for the material use of its inherent carbon is gasification. Traditional gasification processes are often autothermal or require the combustion of part of the biomass feedstock to provide the energy required for the gasification and pyrolysis reactions. This leads to a loss of carbon in the form of CO_2 which should be avoided for maximum carbon conversion into syngas. A possible solution is the operation of the gasification process with plasma assistance. In this way, the energy for gasification and pyrolysis reactions is provided through electricity input and higher quality syngas at higher carbon efficiencies can be produced. One type of such gasifier which looks promising based on first process simulations in Aspen Plus is a plasma-assisted entrained flow gasifier for steam gasification of pulverized biomass input [2].

While there has been significant progress on understanding entrained flow gasification of pulverized fuels under conventional gasification conditions [3, 4], plasma gasification under entrained flow conditions has only seen very limited research activity so far. Vishwajeet et al [5] have examined the gasification of sewage sludge in plasma-assisted entrained flow gasification conditions using a nitrogen plasma torch in a vertical drop tube reactor. The focus was placed on achieving a proof of concept. Detailed reaction mechanisms such as, e.g., char burnout behaviour and char reactivity were not studied. As these characteristics are essential for modelling of plasma-assisted entrained flow gasification and, therefore, need to be in place for the simulation-based design of these gasifiers, research into char properties after plasma entrained flow conditions is necessary. For this purpose, the authors have designed a horizontal entrained flow plasma gasification test rig to produce plasma pyrolysis chars for examination in thermogravimetric analysers and characterization. The design of the test rig consists of a horizontal water-cooled tubular reactor with a concentrically positioned DC plasma torch as shown in Figure 1. Pulverized biomass is fed from the top via a ceramic tube into the plasma zone created by the plasma torch. After leaving the plasma zone, the produced char falls onto a solids extraction tool which can be removed from the tubular reactor after the experiments are finished. This makes it possible to study char characteristics of this char created under plasma entrained flow conditions.

https://doi.org/10.52202/069564-0047

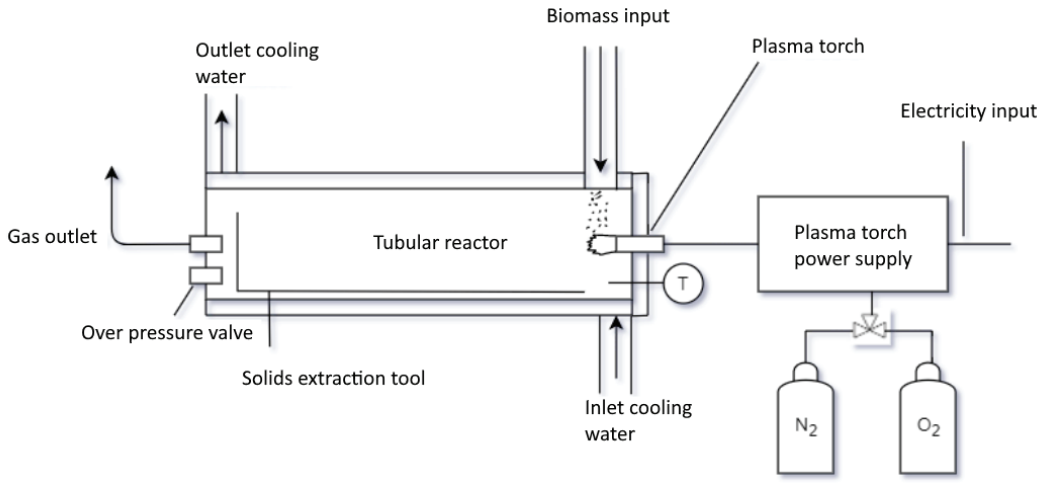

Figure 1. Schematic overview of the tubular plasma gasification test rig for biomass conversion into char under plasma-assisted entrained flow conditions.

In order to produce the highest quality plasma pyrolysis chars, the pulverized fuel needs to mix as well as possible with the plasma zone of the plasma torch resulting in very high heating rates and as high as possible particle temperatures. This leads to two research questions which this research aimed at through computational fluid dynamics simulation of the reactor setup: How can the reactor be modified to improve particle mixing and heating in the plasma zone? At which distance from the plasma inlet should particles be injected to maximize heat transfer to the fuel particles?

Therefore, this research not only helps optimizing the design of the plasma gasification test rig, it also adds to the existing literature on CFD for plasma gasification/pyrolysis because existing CFD research in this area has mainly focussed on fixed bed, downdraft or updraft plasma gasifiers instead of entrained flow reactor setups [6–9].

To answer the research questions, the following cases were simulated in Ansys Fluent:

- Case 0: **1 mm** plasma torch nozzle diameter, free vertical particle drop 40 mm from torch outlet
- Case 1: **2 mm** plasma torch nozzle diameter, free vertical particle drop 40 mm from torch outlet
- Case 2: 2 mm plasma torch nozzle diameter, vertical particle inlet tube **5 mm** from plasma torch outlet
- Case 3: 2 mm plasma torch nozzle diameter, vertical particle inlet tube **15 mm** from torch outlet
- Case 4: 2 mm plasma torch nozzle diameter, vertical particle inlet tube **25 mm** from torch outlet
- Case 5: 2 mm plasma torch nozzle diameter, vertical particle inlet tube **35 mm** from torch outlet

Section 2 presents an overview of the methodology behind the simulations for these cases. Section 3 details how the geometry for the model was generated and presents the mesh independence study. Section 4 goes into detail on the simulation results for the different cases by presenting the results and discussing them. Section 5 finishes with the conclusion and outlook into future research opportunities.

2. CFD modelling methodology

The CFD simulation of the reactor was performed using Ansys Fluent. The CFD model simulates the plasma gas, in this case air, as a single high temperature fluid neglecting species created by the plasma through ionization, dissociation, etc. The pulverized biomass particles, in this case torrefied wood particles, are simulated with the help of a discrete phase model with the Eulerian-Lagrangian approach [10]. Ionization and dissociation of air in the single fluid model is covered with the help of adjusted plasma air properties. Chemical reactions involving the torrefied wood particles have been neglected as the major focus of the created model is on assessing the mixing behaviour and heat transfer between the hot plasma gas zone and the particles.

2.1. Air plasma properties

The adjusted plasma air properties are retrieved from curve fits calculated by Gupta et al. [11] for a temperature range of 1,000-30,000 K. The study considers 11 species while neglecting real-gas interactions and radiation effects. The plasma torch manual [12] specifies the power range as well as the temperatures of the arc plasma. At an operating temperature of $T_P = \sim 17 \cdot 10^3\ K$, the gas composition varies drastically from undissociated air. Table 1 compares the mole fractions of species at temperatures lower than 1,000 K, 5,000 K and 17,000 K.

https://doi.org/10.52202/069564-0047

Table 1. Mole (X) and mass (w) fractions of air components at atmospheric pressure for different temperatures, adapted from [13].

		N_2	O_2	N	O	N^+	O^+	e^-
Temperature /K	M /g/mol	28.01	32.00	14.01	16.00	14.01	16.00	5.49e-4
<1,000	X	0.78	0.21					
	w	0.76	0.23					
5,000	X			0.23	0.08	0.29	0.08	0.03
	w			0.34	0.14	0.43	0.10	1.63e-6
17,000	X			0.09	0.03	0.35	0.09	0.45
	w			0.16	0.06	0.61	0.17	3.07e-5

As the mole fractions were read off a logarithmic diagram provided by Selle [13], the values remain somewhat inaccurate. This realization arose when later computing the ionization degree using three different equations from [14]:

$$\alpha_i = \frac{1-X_A}{1+X_A} = \frac{X_{A+}}{1-X_{A+}} = \frac{X_{e-}}{1-X_{e-}} \tag{1}$$

where x_A, x_{A+} and x_{e-} denote the molar fraction of (dissociated) neutral species, ionized species and electrons, respectively. This yields $\alpha_i \in [77\%, 83\%]$ and thus a maximum deviation of 5.9%, which was accepted for further calculations.

In the material dialogue box in Ansys Fluent, properties can be adapted in many ways: Aside from the defined gas models (ideal gas, real gas, kinetic theory...), there are user-defined options as well. To transfer the curves from Gupta et al. [11] to Fluent, two of those were tried out; the first being the piecewise polynomial and the second the user defined function (UDF). The UDF option resulted in a much less stable simulation, forcing the authors to go for the piecewise polynomial option for specific heat capacity, thermal conductivity, and viscosity. Since Gupta et al. [11] provide no graph for the density, it had to be computed.

2.2. Model choice and assumptions

As the pressure-based solver is more suited for thermochemical conversion (e.g., combustion, …) cases and offers many advantages over the density-based solver, it was chosen and combined with the energy and discrete phase models for all simulations of the plasma entrained flow gasification test rig. The flow was assumed to be steady while particles are unsteady by default. The model has also only been tested using inert wood particles, which by definition do not exchange mass with the gas and follow the laws of inert heating and cooling [15]. Since this mass exchange is the main source of energy and momentum transfer, the study deals with a one-way coupling case and so, no interaction with continuous phase was needed. Instead, the Discrete Random Walk Model was activated for all cases because it produces much more realistic tracks. As the turbulence at the wall boundary are of less interest, the k-ω-model and its related SST-models were excluded for this study. Instead, the standard k-ϵ-model was selected, for it is better at modelling the bulk phase than the former and simpler than the latter. This model choice is also supported by Bobzin et al. [16], who examine an argon arc plasma spray using Ansys-CFX and classify it as a "valid alternative". There, the k-ω-model yields fairly different profiles of the arc plasma than all other investigated models. As a simplification, radiation effects are not considered as the focus of this simulation is mainly on the mixing behaviour of fuel particles and plasma zone as indicated by particle temperatures.

2.3. Boundary conditions

This section explains which boundary conditions as well as particle variables were set for the simulations. An overview of all values can be found in Table 2, Table 3, and Table 4.

2.3.1. Inlet

To determine the mass flow rate, the energy equation (2) was applied to the plasma torch represented as an electric heater and subsequent nozzle as depicted in Figure 2:

$$\frac{d}{dt}(U + K + \phi) = \sum_j \dot{m}_j \left(h_j + k_j + \phi_j\right) + \sum_j \dot{Q}_j + \dot{W}_V + \dot{W}_s \tag{2}$$

where the upper case variables U, K and ϕ denote the internal, kinetic and potential energy, respectively, while the equivalent lower case letters signify their specific forms for the different components j. h_j represents the specific enthalpy of component j. Furthermore $\dot{m}$ stands for the mass flow rate, $\dot{Q}$ for the heat flux and $\dot{W}_V + \dot{W}_s$ (volume change and shaft work) for the technical work.

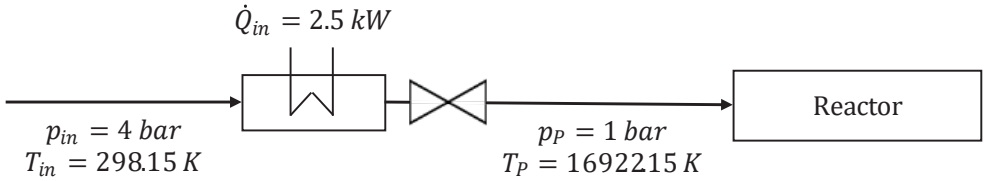

Figure 2. Simplified representation of plasma torch as thermodynamic process leading to plasma inlet: Temperature T and pressure p before (in) and after (P) power input $\dot{Q}_{in}$.

The subscripts in and P denote the states at the inlet of the heater and the outlet of the plasma torch, respectively. Compressed air enters at an operating pressure of $p_{in} = 4\ bar$ [12] and an assumed temperature of $T_{in} = 300K$. It then flows isobarically through the plasma torch that is connected to a power supply and is expanded after the plasma torch, which is illustrated as a nozzle in Figure 2. Through this abrupt (ideally isentropic) expansion, the pressure is reduced back to atmospheric pressure ($p_P \approx 1bar$). According to the torch manual [12], the plasma zone is expected to enter the reactor at a core temperature of $T_P = 16922.15K$. For the incoming specific enthalpy, Bernoulli's equation for compressible ideal gases was used without the kinetic term ($h_{in} = c_p \cdot T_{in} + p/p(T_{in})$) [17, 18] while the outgoing specific enthalpy h_P was taken from [11] for $T_P = 16922.15K$. The energy equation was then solved for the velocity at the outlet of the nozzle. To characterize the flow conditions, some dimensionless numbers were calculated: Reynolds number (Re), turbulence intensity (TI) and Mach number (Ma).

As the standard configuration of the plasma torch uses a very small outlet diameter of 1 mm which results in very high outlet velocities with Mach numbers >0.5, it was decided to modify plasma torch nozzle diameter from 1 mm (= case 0) to 2 mm (= case 1, reference case). For this reference case, plasma temperature increases slightly while Mach number and plasma gas velocity drastically decrease (see Table 2).

Table 2. Calculated plasma inlet conditions for varied plasma inlet diameters. For general boundary conditions and torrefied wood properties please refer to Table 3 and Table 4 respectively.

Case	0 (Smaller diameter)	1 (Reference)
d_P /[mm]	1.00	2.00
T_P /[K]	16922.15	17193.74
v_P /[m/s]	3561.33	917.65
$\dot{m}$ /[g/s]	1.60E-2	1.60E-2
Ma /[-]	0.58	0.15
Re /[-]	7.53E+5	3.18E+5
TI /[%]	2.95	3.28

2.3.2. Gas outlet

As the gas outlet at the end of the reactor is a pressure outlet where internal and atmospheric pressures can be assumed to be roughly equal, the gauge pressure was set to zero and the backflow temperature to 360 K, which was the mass weighted average of total temperature at the outlet from an initial simulation. By also using the mass weighted average of velocity in z-direction at the outlet, the turbulence intensity was determined. The outlet variables are listed in Table 3 and were used for all cases.

2.3.3. Reactor wall

The wall thickness of the reactor's stainless steel wall was set to 2.5 mm [19] with a heat generation rate $\dot{Q}_{gen}$ of 0 W/m3. Since shell conduction treats the boundary as a thin wall [20] and disables the wall material specification, which is important for heat transfer phenomena, it was deactivated. It was assumed that the heat transfer rate from the cooling water to the reactor wall is much greater than that of air inside the reactor to the reactor wall. Thus, it was assumed that the wall temperature is constant at 293.15 K. The wall boundary conditions are summarized in Table 3.

Table 3. General boundary conditions.

	Plasma inlet	Particle inlet		Outlet		Reactor wall
d_P /[mm]	2.00	5.00	d_{out} /[mm]	26.00	d_{wall} /[mm]	2.5
T_P /[K]	17193.74	298.15	$T_{Backflow}$ /[K]	358.43	T_{wall} /[K]	293.15
$\dot{m}$ /[g/s]	1.60E-2	2.34E-1	p_{gauge} /[Pa]	0	$\dot{Q}_{gen}$ /[W/m³]	0
TI /[%]	3.28	2.50	TI /[%]	2.49	Shell cond.	no

https://doi.org/10.52202/069564-0047

2.3.4. Particle injections

The simulated torrefied wood particles have a density of $\rho = 700kg/m^3$, a lower heating value of $LHV = 19.855MJ/kg$ and a specific heat capacity of $C_p = 2310J/kgK$ based on previous lab analysis. The mass flow rate of the torrefied wood particles was determined by specifying that the plasma power should make up 50% of the lower heating value input of the wood particles. This is typically the maximum required plasma power input to operate under pure allothermal plasma gasification conditions for comparable feedstocks [2]. Based on this assumption, the mass flow of wood particles were calculated resulting in the values indicated in Table 3. The wood particles were assumed to have a particle size distribution as shown in Table 4.

Table 4. Torrefied wood injection settings for Discrete Random Walk Model.

Inert Wood Particles					
d_{min}	/[m]	9E-5	T_{BM}	/[K]	298.15
d_{max}	/[m]	1.1E-4	v_{BM}	/[m/s]	10.31
d_{mean}	/[m]	1E-4			

3. Geometry and mesh generation

The first step of the CFD simulation of the plasma entrained flow gasification test rig was to create a geometry and mesh which is mesh independent for an acceptable level of deviation from the benchmark mesh. The target was to accept a maximum deviation from the benchmark mesh of 10%. A lower deviation level is not required because the simulations serve the purpose of informing the optimization of the experimental set-up. Maximum accuracy is not necessary for this purpose.

3.1. Mesh

The reactor design as shown in Figure 1 was recreated using SpaceClaim. The first step was to simplify the constructed plasma-jet-tube configuration down to what is essential for Fluent calculations, so the cooling jacket, the tubular viewing window and all external components were neglected. Running the first few simulations showed that the posterior section of the 1.5 m long reactor had no influence on results and was hence cut off to reduce computational time.

To generate the mesh, several tubular bodies of influence (BoI) were defined for each section of the tube: Starting from the smallest grid cell size x_{min} at the plasma inlet, the mesh was gradually coarsened along the tube as demonstrated in Figure 3. Since the chosen mesh type is poly-hexcore, the octree meshing algorithm had to be taken into account when conducting the sensitivity study, so that they do not get set arbitrarily during meshing. Therefore, the target cell size x of each refinement level had to fulfil the relation:

$$x = x_{min} \cdot 2^t \tag{3}$$

where x_{min} denotes the smallest cell length (in this case: at the plasma zone refinement), and t the number of transition layers from x_{min} to x_{max}. The plasma zone's BoI includes the sharpest part of the plasma zone and is supported by a face of influence with the same cell size at the inlet boundary.

The starting point for x_{min} was inspired by Wilhelm [21], where a mesh refinement of 10 cells per diameter was used. The following relation has proven to be sufficiently accurate in his case:

$$d_c = \sqrt{\frac{A(d_c)}{A(d_i)}} \cdot d_i \tag{4}$$

For an inlet diameter of $d_i = 1mm$ and a cell diameter of $d_c = d_i/10$, the resulting minimum cell size was 0.1mm (case C). From there on, the other cell sizes were derived. Then x_{min} along with its other cell sizes were reduced to create the different cases for the mesh independence study as shown in Table 5.

3.2. Mesh independence study

After performing the simulations for the mesh independence study using the mesh parameters as detailed in the previous section, the velocity magnitude and total temperature were evaluated along the reactor length for each refinement level and compared to the most detailed reference case A. This yields the discrepancies plotted in Figure 4 along the significant part of reactor.

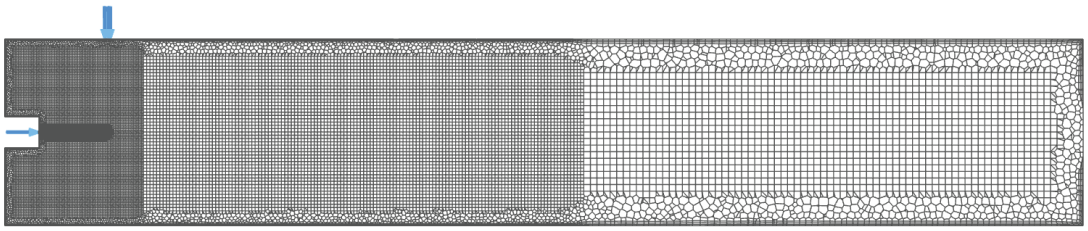

Figure 3. Poly-Hexcore mesh of reactor tube (coarsened to xmin = 0.12mm for visibility).

Table 5. Mesh independence study: Cell lengths x /[mm] for each body of influence of transition layer t.

BoI t	Plasma zone 0	Anterior 3	Middle 4	Posterior 5	Total cells
A	0.06	0.48	0.96	1.92	9,772,469
B	0.08	0.64	1.28	2.56	4,301,751
C	0.10	0.80	1.60	3.20	2,274,814
D	0.12	0.96	1.92	3.84	1,370,240

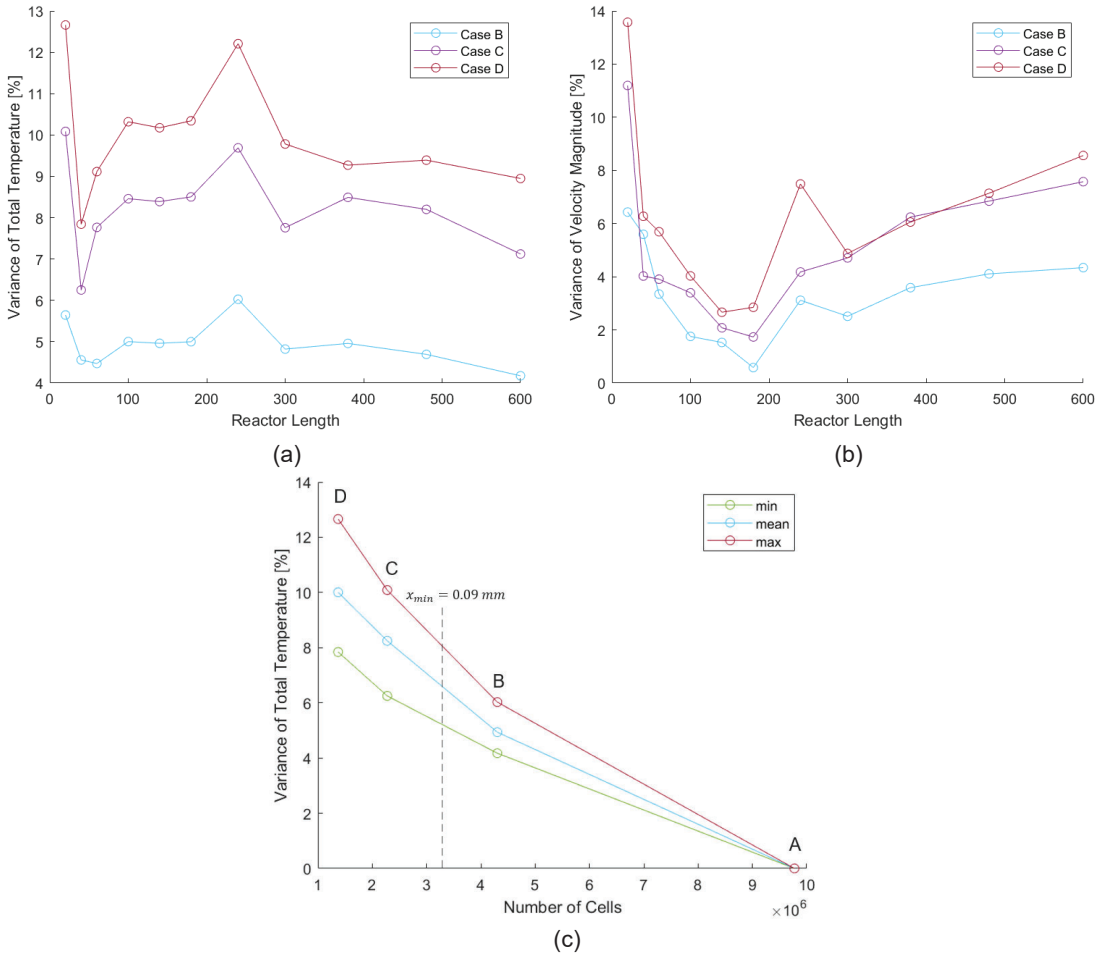

Figure 4. Mesh independence study for mesh cases A, B, C and D. (a) Total temperature error along the reactor length in mm for cases B, C and D relative to case A. (b) Velocity magnitude error along the reactor length in mm for cases B, C and D relative to case A. (c) Mean, minimum and maximum error of velocity magnitude along the reactor length as a function of the number of cells for meshes A, B, C and D.

https://doi.org/10.52202/069564-0047

Due to the high inlet velocity of the plasma gas and the sharp temperature gradients, one can see the highest variance at the inlet (20 mm from reactor inlet) and another peak in the middle. A possible explanation for the peak in the middle could be that the solution seems to start at the boundaries and spreads throughout the reactor with more iterations. As mass-weighted variables have not been tracked at each measurement point during the simulation, the properties at this position of the reactor might not have plateaued yet. Supporting this explanation is the fact that this peak is farther away from the outlet of the reactor's mesh (630 mm from reactor inlet) where the cell size is larger, so the converged solution is reached quicker. Also, the mass imbalance is comparatively higher at this position.

Because the velocity magnitude shows higher variability than the temperature, it has been chosen as the determining factor for the final mesh size; its minimum, maximum and mean values are plotted against the cell number in Figure 4 (c). Weighing computation expenses against solution accuracy led to the decision, that a refinement level of $x_{min} = 0.09\,mm$ should suffice to keep the maximum deviation from mesh A below 10%.

Based on this mesh independence study, a slightly modified final mesh B' was created using the mesh B as the basis. This resulted in the mesh data as shown in Table 6 and made it possible to reduce the required number of cells by ~28% compared to mesh B.

Table 6. Modified mesh refinements: Cell lengths x /[mm] for each body of influence of transition layer t.

BoI t	Plasma zone 0	Anterior 3	Middle 4	Posterior 5	Total cells /[%]
B	0.08	0.64	1.28	2.56	100
B'	0.09	0.72	1.44	2.88	71.80

4. Results and discussion

4.1. Cases overview

The first two cases, case 0 and case 1, which were assessed, only vary geometrically in terms of the outlet diameter of the plasma torch nozzle as shown in Table 2.

The other cases focus on the way in which the biomass particles are introduced to the plasma zone. Case 1, and also case 0, assume a simple opening at the top of the reactor's tube through which biomass particles can be sent into the reactor. To examine the direct effect of plasma on biomass particles, the particle inlet was brought closer to the plasma zone with the help of a vertical particle inlet tube, which was integrated at different distances from the plasma torch outlet for the cases 2 to 5. The job of the vertical particle inlet tube was to guide the biomass particles as close to the plasma zone as possible. Assuming the tube is made from high-temperature resistant ceramic material, its length l_{tube} was determined, so that it does not meet temperatures exceeding 1500 K. To obtain the plasma zone's temperature profile, the particle inlet was defined as a wall and its mass flow rate, turbulence intensity as well as hydraulic diameter were set to 0, so that the flow is not affected by cold incoming air. The injected particles were also defined as massless. The distance of the vertical particle inlet tubes from the plasma torch outlet was then varied along the 1500 K isotherm. The resulting inlet tube positions for the cases 2 to 5 and case 1 as the reference are listed in Table 7.

Table 7. Geometry parameters for varied particle inlet tube lengths l_{tube} and distance of the particle inlet tube from the plasma torch outlet s_{tube}. All remaining parameters are based on Table 3 and Table 4.

Cases		1 (reference)	2	3	4	5
l_{tube}	/[mm]	0.00	49.00	46.50	44.50	42.50
s_{tube}	/[mm]	40.00	5.00	15.00	25.00	35.00
$d_{part,in}$	/[mm]	5.00	5.00	5.00	5.00	5.00

4.2. Cases 0-1: Results of plasma torch outlet diameter variation

The main results for cases 0 and 1 consisting of average particle temperatures and respective residuals are presented in Figure 5.

Figure 5 (a) shows the average temperature of all particles in a selected time interval for both cases. In case 1, the plasma gas flows in at a velocity of $v_1 = 917.65 m/s$ and a temperature of $T_1 = 17193.74 K$ compared to $v_0 = 3561.33 m/s$ and $T_0 = 16922.15 K$ in the reference case. The conservation of energy explains this increase in temperature, which compensates the reduction in the kinetic term because of the lower plasma gas velocity. Consequently, particles reach average temperatures up to 2.1x higher in case 1 compared to case 0 ($T_{max,0} = 986.534 K$ and $T_{max,1} = 2092.61 K$). They also remain hotter as indicated by higher volume-averaged temperatures ($T_{V,0} = 513.64 K$ and $T_{V,1} = 703.45 K$). Therefore, case 1 performs better than case 0 at achieving a good mixing between biomass particles and the hot plasma gases in the plasma zone.

https://doi.org/10.52202/069564-0047

The residuals also indicate that convergence for case 0 is worse than convergence for case 1. Due to the increased mass flow rate and thereby also velocity gradient at the inlet, the solution does not converge as smoothly for case 0. Despite the enlargement of the plasma zone and anterior bodies of influence and using a finer mesh than the initial one (0.08 mm), the continuity remains above 10^{-3} for case 0 as shown in Figure 5 (b). Furthermore, the volume-averaged velocity oscillates around $v_{V,0} \approx 0.7m/s \pm 0.03m/s$ while temperature stagnates at $T_{V,0} \approx 520K$. This behaviour could be explained by one of three potential causes; the first one being the mesh, the second one under relaxation factors and the third being the complexity of the flow:

1. The mesh might still not be sufficiently fine in some areas of the reactor. The higher inlet velocity also leads to increased velocities in other parts of the reactor.
2. Under-relaxation factors (URFs) were varied differently for both cases, which could justify this behaviour.
3. Because of the complexity of the flow, a unique solution might simply not exist. As the solution of the flow is steady, it is very likely to have more than one solution for the same boundary conditions. This would justify why properties oscillate periodically between two possible states.

As case 1 performed better in terms of both the average particle temperatures, as a proxy of the quality of mixing between particles and plasma zone, and convergence, the worse convergence of case 0 was not further studied. Instead, it was decided, as already indicated in section 2.3.1 due to the lower plasma gas velocities, to continue with case 1 as the base case for the further improvement of the reactor.

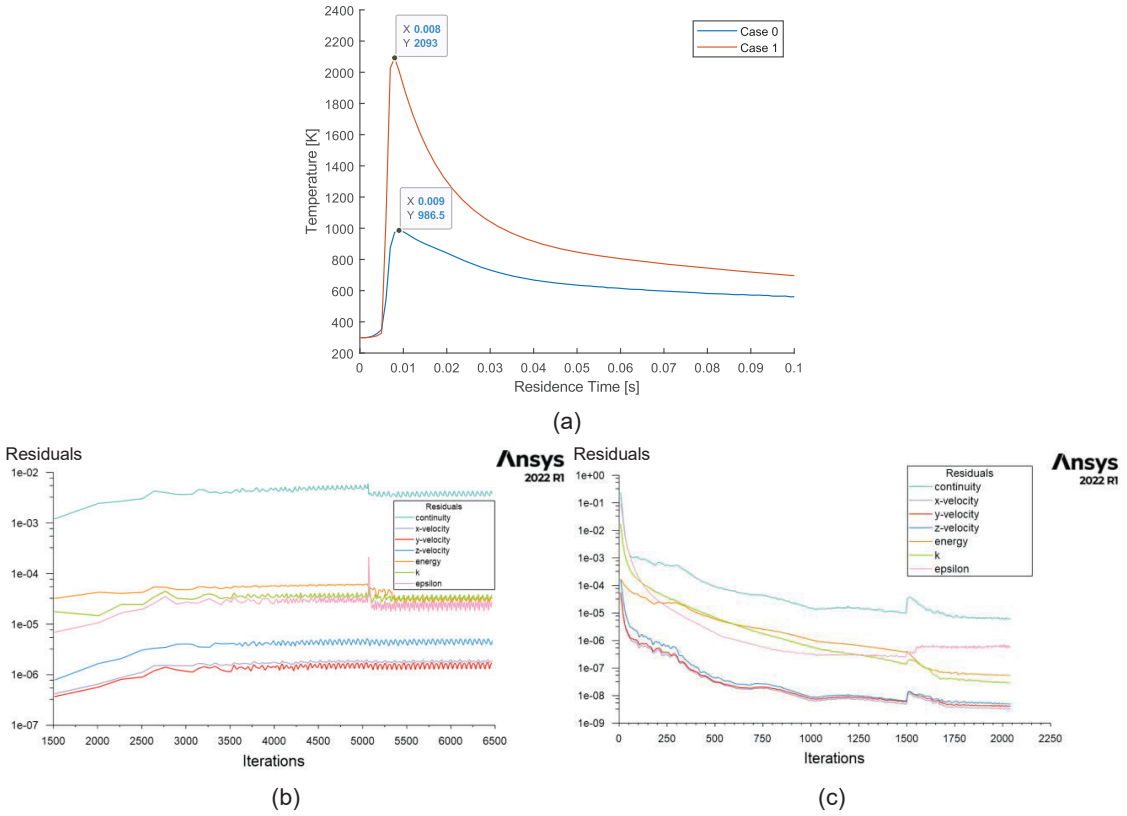

Figure 5. Comparison of residuals and average particle temperatures of cases 0 and 1. (a) Average particle temperatures over residence time for cases 0 and 1. (b) Residuals of case 0. (c) Residuals of case 1.

4.3. Cases 1-5: Results of variation of particle inlet tube's position

The intention behind varying the tube position is to find the configuration where particles reach the highest temperatures and maintain them for the longest period. Figure 6 shows the average particle temperatures plotted over the residence time. For each case, the mean value of all temperatures in a specified time interval were evaluated using Matlab and then plotted with the other cases. Figure 7 compares particle temperatures and their tracks for the different cases. The graphs of the two figures clearly indicate that cases 2 and 3 perform better in terms of maximum (average) temperature compared to the other cases which do not exceed 2200K. This is essentially a consequence of the extreme temperatures particles come in contact with in the core

https://doi.org/10.52202/069564-0047

plasma zone, which reach up to 15,000K and 7,500K, respectively. The higher deflection angle of the plasma zone might also improve the particle heating, as higher temperatures are shifted downwards towards the particle tracks and thus heat them longer. High collision velocities also cause particles to be distributed better in cases 2 compared to other cases. As previously established by Gupta et al. [11], the higher thermal conductivity at such temperatures is higher and therefore particle heating is improved even more significantly as shown in Figure 6 (a). The delayed peak in case 1 is due to the fact that particles have to travel longer from the top of the reactor before hitting the flame – while the residence time only starts counting in cases 2 to 5 when the particles exit the ceramic tube close to the plasma zone. The slight bump in cases 4 and 5 may be a consequence of high turbulence in that time interval, which could be deduced from the particle tracks. But it may also be a consequence of incomplete convergence.

When looking at the long-term particle temperatures in Figure 6 (b), case 5 surpasses the other cases, even if only slightly. Looking at the particle path lines, it gets clear that this is because particles fly back into the plasma region and are thereby reheated. However, particles in all cases do not maintain a high temperature after the sharp decline down from the peak. This goes back to the relatively low overall temperature of the gasifier. It shows that the particles are quenched rather fast upon leaving the plasma zone reaching temperatures <1000K within <<0.1s in all cases. This is beneficial for the production of plasma pyrolysis char as fast quenching would be helpful in preserving the change of the char properties caused by the plasma zone.

Based on Figure 6 and Figure 7, case 2 looks the most promising. It achieves both a very high peak temperature, indicating a good mixing of particles with the plasma zone, as well as comparatively fast quenching of the particle temperature after the plasma zone.

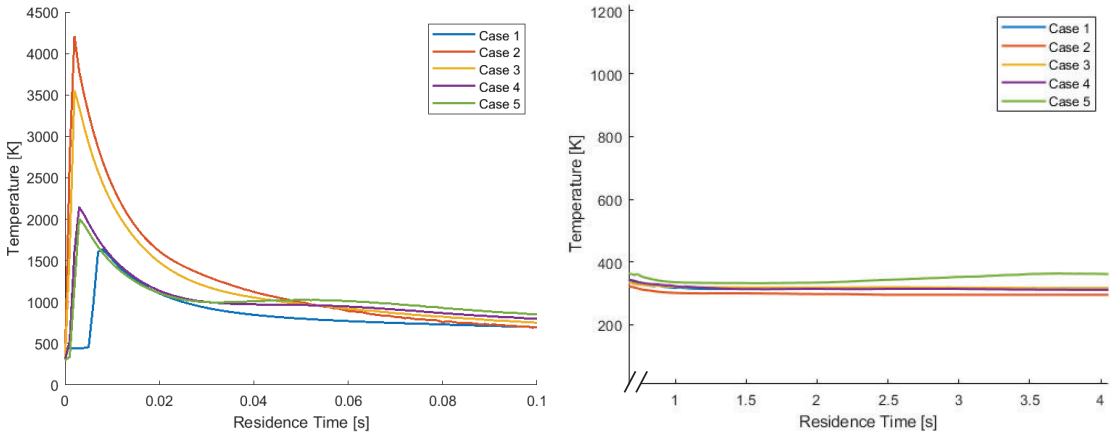

Figure 6. Average particle temperature distribution over residence time for cases 1-5. (a) Average particle temperature peaks during first 0.1 seconds of residence time. (b) Long-term average particle temperatures.

Based on the residuals for cases 2 to 5 in Figure 8 and those of case 1 in Figure 5, the convergence of cases 2, 4 and 5 are far less stable than cases 1 and 3. One reason is the change and increase in the plasma zone upon integration of the plasma tubes (cases 2-5). This means that the plasma zone BoI does not only need to be angled but enlarged as well. For case 2 the instability could be easily explained by the fact that the collision velocities of particles and plasma gas are significantly higher than in all other cases as the particle inlet tube in this case is closest to the plasma torch outlet. Even after modifying the plasma zone BoI in case 2, the residuals still oscillate, but around 10^{-4} to 10^{-3} instead of 10^{-2} before modification. The gradual decrease in the residuals around 2000 iterations (Figure 8 (a)) is a consequence of reduced under relaxation factors, which were improving the solution until approximately 2700 iterations.

https://doi.org/10.52202/069564-0047

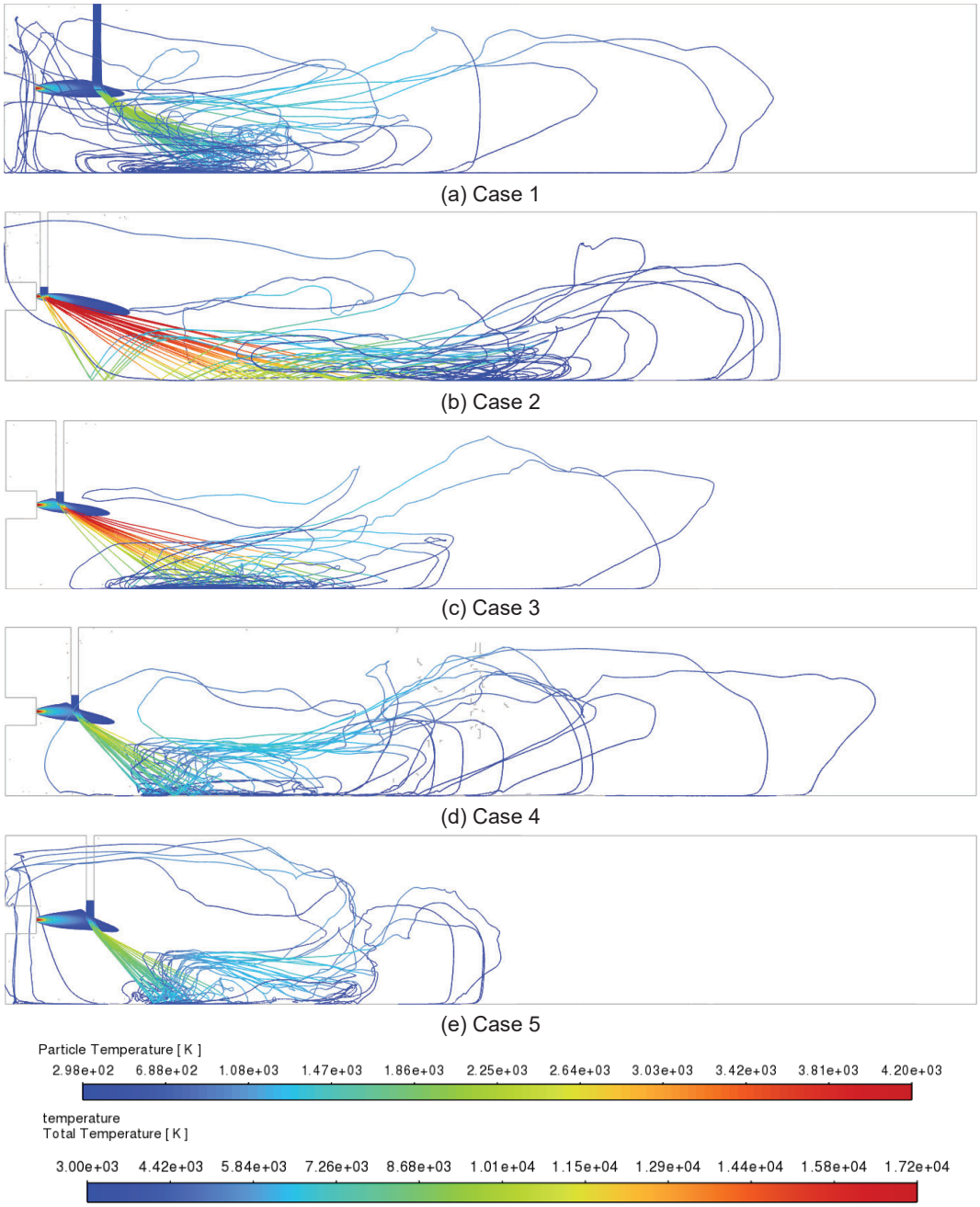

Figure 7. DC arc plasma zone temperature and (inert) torrefied wood particle streamlines coloured based on temperature for cases 1 to 5.

Same applies for cases 4 and 5, where volume-average-temperature and velocity are oscillating periodically around the same range that is computed by case 1. It is only in case 3 where both physical and numerical properties stagnate as shown in Figure 8 (b). Although the same case and data file was used for interpolation at the beginning, this case is far better converging than all three other cases.

However, since all cases oscillate periodically around 10^{-4} to 10^{-3}, the change in solution should not be significant. For example, in case 4: $v_{V,4} \approx 0.7m/s \pm 0.05m/s$ and $T_{V,4} \approx 700K \pm 5K$. The aim of these cases anyway is to reveal the trend of the best tube position for particle mixing and heating, which would not be heavily affected by oscillations at such a comparatively small magnitude. As long as the physical phenomena make sense, which they do in all of those cases, the result should be valid.

https://doi.org/10.52202/069564-0047

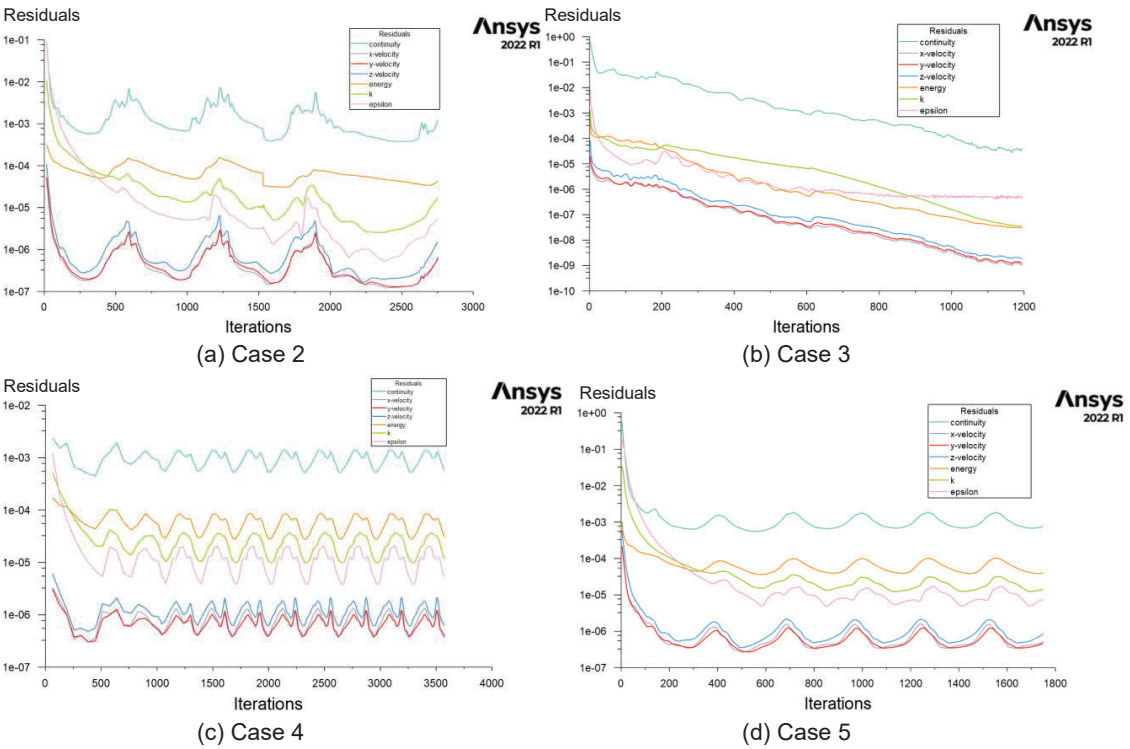

Figure 8. Residuals of cases 2-5 vs. number of iterations.

5. Conclusion

This work has investigated the flow characteristics of a DC air plasma torch in a horizontal tube reactor and investigated different optimization options to improve the interaction of biomass particles with the plasma zone. Plasma gas properties were modelled by integrating the adjusted plasma air properties provided by Gupta et al. [11]. Simplifying assumptions were made to ensure the feasibility of the CFD model – among others, neglecting chemical reactions, assuming a single fluid model and ignoring heat exchange by radiation. The different optimization options which were assessed focused on the one side on changing the plasma torch's outlet nozzle diameter to adjust plasma gas velocities and on the other side the integration of vertical biomass particle inlet tubes to better guide the fuel particles directly into the plasma zone (at distances 5, 15, 25 and 35 mm from the torch outlet along the isotherm of 1500 K). It can be concluded that the wider diameter offers not only better convergence, but much higher particle temperatures as well. From all conducted cases, the closest tube to the plasma inlet (case 2) leads to the highest particle temperatures. Cases 4 and 5 do not seem to offer a significant advantage over case 1 without a tube. All cases exhibit comparatively fast quenching (<<0.1s) of the particle temperatures after the plasma zone, which is beneficial for producing plasma pyrolysis char for further experimental analysis. In addition, all cases (except for case 5) show the same long-term cooling behaviour. The deciding factor for the best configuration to enhance particle heating is therefore only highest average temperatures, which was demonstrated in case 2 followed by case 3.

The created CFD simulation model is a good starting point for further research into modelling of plasma-assisted entrained flow gasification. In subsequent models, it would make sense to look into the option of changing the single fluid model to a more sophisticated plasma representation also accounting for dissociated and ionized, highly reactive species. For this, it would also be beneficial to integrate chemical reactions into the model as well as radiative heat transfer to better simulate the processes happening in the high temperature zones. In this regard, a combination with other existing CFD models for conventional entrained flow gasification such as the model developed by DeYoung [10] will be a suitable next step. In addition, experimental data will be necessary to inform the modelling and create kinetic models for the simulation of these plasma gasification processes. Experimental results from the modelled test rig can also be used to validate the simulative results.

Acknowledgments

This study was carried out in the framework of the EU Horizon 2020 project "TWIN-PEAKS" (project no.: 951308) funded by the European Union and the International Future Lab on Green Hydrogen Technologies "REDEFINE Hydrogen Economy (H2E)" (project no.: 01DD21005) sponsored by the Federal Ministry for Education and Research (Germany). The financial support is gratefully acknowledged.

Nomenclature

c	specific heat, J/(kg K)
d	diameter, mm
h	heat transfer coefficient, W/(m² K)
$\dot{m}$	mass flow rate, kg/s
p	pressure, Pa
t	transition layer
v	velocity, m/s
x	cell length, mm
A	area, m²
BoI	Body of Influence
CFD	Computational Fluid Dynamics
DC	direct current
K	kinetic energy, kJ
LHV	lower heating value, MJ/kg
Ma	Mach number
Re	Reynolds number
TI	turbulence intensity
T	temperature, °C or K
UDF	user defined function
U	internal energy, kJ
W	work, kJ
α	ionization degree
ϕ	potential energy, kJ
ρ	density, kg/m³

References

[1] M. Carus, F. Kähler, and O. Porc, *Global Carbon Demand for Chemicals and Derived Materials: Global Carbon Demand for Chemicals and Derived Materials in 2020 and Scenario for 2050 in million of embedded carbon.* [Online]. Available: https://renewable-carbon.eu/publications/product/global-carbon-demand-for-chemicals-and-derived-materials-png/ (accessed: Mar. 25 2023).

[2] S. Bastek, M. Kerschbaum, M. Dossow, S. Fendt, and H. Spliethoff, “Process Simulation of Plasma-Assisted Entrained Flow Gasification for Hydrogen-rich Syngas Production,” in *2022 International Freiberg Conference on Waste Gasification*, Freiberg, 2022.

[3] T. Netter, A. Geißler, and H. Spliethoff, “Determination of the Intrinsic Gasification Kinetics of a Bituminous Coal Including Product Gas Inhibition and Char Deactivation Under Entrained Flow Conditions,” *Journal of Energy Resources Technology*, vol. 142, no. 7, 2020, doi: 10.1115/1.4046142.

[4] T. Netter, S. Fendt, and H. Spliethoff, “A collection of model parameters describing the gasification behavior of different fuels under entrained flow conditions,” *Fuel*, vol. 296, p. 120536, 2021, doi: 10.1016/j.fuel.2021.120536.

[5] Vishwajeet *et al.,* “Entrained Flow Plasma Gasification of Sewage Sludge–Proof-of-Concept and Fate of Inorganics,” *Energies*, vol. 15, no. 5, p. 1948, 2022, doi: 10.3390/en15051948.

[6] M. Sakhraji, A. Ramos, E. Monteiro, K. Bouziane, and A. Rouboa, “Plasma gasification process using computational fluid dynamics modeling,” *Energy Reports*, vol. 8, pp. 1541–1549, 2022, doi: 10.1016/j.egyr.2022.08.069.

[7] S. Choi, “Numerical Simulation of Thermal Plasma Gasification Process,” *AMM*, 799-800, pp. 90–94, 2015, doi: 10.4028/www.scientific.net/AMM.799-800.90.

[8] F. Rojas-Perez, J. A. Castillo-Benavides, G. Richmond-Navarro, and E. Zamora, “CFD Modeling of Plasma Gasification Reactor for Municipal Solid Waste,” *IEEE Trans. Plasma Sci.*, vol. 46, no. 7, pp. 2435–2444, 2018, doi: 10.1109/TPS.2018.2844867.

[9] N. K. C. Qing, N. A. Samiran, and R. A. Rashid, “CFD Simulation Analysis of Sub-Component in Municipal Solid Waste Gasification Using Plasma Downdraft Technique,” *CFDL*, vol. 14, no. 8, pp. 63–70, 2022, doi: 10.37934/cfdl.14.8.6370.

[10] S. DeYoung, “Numerical simulation of entrained flow gasification with focus on char reaction kinetics,” Dissertation.

[11] R. Gupta, K.-P. Lee, R. Thompson, and J. Yos, *Calculations and curve fits of thermodynamic and transport properties for equilibrium air to 30000 K*: NASA, 1991.

[12] Parkside, *PLASMA CUTTER PPS 40 B2*.

[13] S. Selle, “Transportkoeffizienten ionisierter Spezies in reaktiven Strömungen,” PhD-thesis, Universität Heidelberg, Heidelberg, Deutschland, 2002.

[14] M. Capitelli, G. Colonna, and A. D’Angola, *Fundamental Aspects of Plasma Chemical Physics*. New York, NY: Springer New York, 2012.

[15] ANSYS Inc., *ANSYS FLUENT 12.0 Theory Guide.* [Online]. Available: https://www.afs.enea.it/project/neptunius/docs/fluent/html/th/main_pre.htm

[16] K. Bobzin, M. Öte, J. Schein, S. Zimmermann, K. Möhwald, and C. Lummer, “Modelling the Plasma Jet in Multi-Arc Plasma Spraying,” *J Therm Spray Tech*, vol. 25, no. 6, pp. 1111–1126, 2016, doi: 10.1007/s11666-016-0438-0.

[17] W. Polifke and F. Schilly, *Engineering Thermodynamics*.

[18] A. Sasoh, *Compressible Fluid Dynamics and Shock Waves*. Singapore: Springer Singapore, 2020.

[19] C. Kranig, “Auslegung und Konstruktion eines Plasmapyrolyseteststands,” Semesterarbeit, Technische Universität München, Deutschland, 2022.

[20] ANSYS Inc., *ANSYS FLUENT User’s Guide: 2022R1*.

[21] S. Wilhelm, “Stationary CFD Simulation of High Temperature Fuel Cell Stacks,” Master's thesis, Technische Universität München, Germany, 2020.

https://doi.org/10.52202/069564-0047